remote sensing

Article

Analysis of Space-Based Observed Infrared Characteristics of Aircraft in the Air

Jiyuan Li [1], Huijie Zhao [1,2], Xingfa Gu [1,3,4], Lifeng Yang [4,5,6], Bin Bai [5], Guorui Jia [1,*] and Zengren Li [1]

1 School of Instrumentation and Optoelectronic Engineering, Beihang University, Key Laboratory of Precision Opto-Mechatronics Technology, Ministry of Education, 37# Xueyuan Road, Haidian District, Beijing 100191, China
2 Institute of Artificial Intelligence, Beihang University, 37# Xueyuan Road, Haidian District, Beijing 100191, China
3 Aerospace Information Research Institute, Chinese Academy of Sciences, 9# Dengzhuang South Road, Haidian District, Beijing 100094, China
4 University of Chinese Academy of Sciences, 9# Dengzhuang South Road, Haidian District, Beijing 100094, China
5 Beijing Institute of Remote Sensing Information, 6# Waiguan Slanting Street, Chaoyang District, Beijing 100011, China
6 Key Laboratory of Intelligent Infrared Perception, Shanghai Institute of Technical Physics, Chinese Academy of Sciences, 500# Yu Tian Road, Shanghai 200083, China
* Correspondence: jiaguorui@buaa.edu.cn

Abstract: The space-based infrared observatory of aircraft in the air has the advantages of wide-area, full-time, and passive detection. The optical design parameters for space-based infrared sensors strongly rely on target observed radiation, but there is still a lack of insight into the causes of aircraft observation properties and the impact of instrument performance. A simulation model of space-based observed aircraft infrared characteristics was constructed for this provision, coupling the aircraft radiance with background radiance and instrument performance effects. It was validated by comparing the model predictions to data from both space-based and ground-based measurements. The validation results reveal the alignment between measurements and model predictions and the dependence of overall model accuracy on the background. Based on simulations, the radiance contributions of aircraft and background are quantitatively evaluated, and the detection spectral window for flying aircraft and its causes are discussed in association with instrumental performance effects. The analysis results indicate that the target-background (T-B) contrast is higher in the spectral ranges where aircraft radiation makes an important contribution. The background radiance plays a significant role overall, while the observed radiance at 2.5–3μm is mainly from skin reflection and plume radiance. The skin-reflected radiation absence affects the model reliability, and its reduction at nighttime reduces the T-B contrast. The difference in T-B self-radiation and the stronger atmospheric attenuation for background contribute to the higher contrast at 2.7 μm compared to the other spectral bands.

Keywords: aircraft infrared observability; spaced-based infrared imaging; radiance components analysis; instrument performance effect

Citation: Li, J.; Zhao, H.; Gu, X.; Yang, L.; Bai, B.; Jia, G.; Li, Z. Analysis of Space-Based Observed Infrared Characteristics of Aircraft in the Air. *Remote Sens.* **2023**, *15*, 535. https://doi.org/10.3390/rs15020535

Academic Editor: Yunhao Chen

Received: 26 November 2022
Revised: 5 January 2023
Accepted: 12 January 2023
Published: 16 January 2023

1. Introduction

The airplane's invention revolutionized how humans travel, connecting faraway places worldwide. The state of the aircraft during navigation has received extensive attention [1], which is the need for economic development and the focus of national defense construction. In today's complex aviation environment, no single technology can yet track all aircraft types in terms of global coverage [2]. Space-based infrared imaging enables the acquisition of aircraft location information on a global scale without time constraints. There is currently no on-orbit infrared instrument designed for flying aircraft detection. The optical design parameters for space-based infrared sensors and the development of detection algorithms strongly rely on target observed radiation. However, there is still a lack of insight into the causes of aircraft observation properties and the effects of instrument performance.

The measurements can provide real infrared data of the aircraft under certain conditions, but the cost is very high. Accordingly, infrared target simulation modeling has been the focus of research in the military field for a long time [3–7]. Battlefield requirements change with the development of technology. Mahulikar et al. [8–10] discussed the relationship between the infrared radiation level and the locking distance for the infrared modeling of military aircraft and proposed the concept of the infrared cross-section. Coiro [11–13] conducted infrared simulation modeling and sensitivity analysis of civil airplanes and unmanned combat air vehicles. The above methods are mainly used for air-to-air or ground-to-air detection scenarios and need to be refined for use in aircraft detectability assessments under space-based infrared observations. Yuan [14] proposed a multispectral integrated model for sea/cloud background radiation characteristics and analyzed the detection performance for the aircraft plume. Zhu [15] established an all-attitude motion characterization and parameter analysis system for aerial targets. These simulation models do not comprehensively account for the aircraft's observed radiation and lack preliminary validation work under the space-based infrared observation. Parts of the radiation were ignored, such as skin or background radiation. Accordingly, it is essential to establish and initially validate a space-based observed aircraft infrared characteristic model, coupling target radiation with background radiation and instrument performance effects.

In the application analysis of the simulation model, Mahulikar et al. [16–20] analyzed the influence of the internal/external radiation sources, the nozzle area, and the skin emissivity on the detection distance and carried out the optimization of the skin emissivity. The sources of infrared characteristic radiation from aircraft in the wide band (3–5 μm and 8–14 μm) are studied [21]. The concept of modulating the infrared characteristics of an aircraft based on the skin anisotropic emissive characteristics was proposed and verified by simulation [22]. Yuan [23] used the signal-to-noise ratio (SNR) and detection distance to analyze the detection capability of the geostationary infrared imaging system for aircraft plumes. Zhu and Yu et al. [24,25] used the comprehensive signal-to-noise ratio (CSNR) to evaluate the detection performance of infrared systems for the optimization of key parameters. In this literature, metrics such as SNR and CSNR were used to evaluate the detectability of infrared detection systems. Still, they cannot directly tell the influence of infrared radiation characteristics of the target, the background, and the system performance [26]. However, there is still a lack of contribution evaluation of aircraft skin emission radiation, reflected radiation, plume radiation, and background radiation to space-based observation radiation. This is not conducive for an insight into the space-based infrared observational properties of the aircraft and the reasons for their formation.

The ground sampling distance (GSD), the modulation transfer function (MTF), the spectral response function (*SRF*), and the noise equivalent temperature difference (NEΔT) are important performance parameters of the infrared system and also widely known parameters in data applications. In the prior literature [23,24,27], the GSD, detection pixel size, and spectral band of the space-based infrared detection system were studied and analyzed. It was agreed that narrow bands outperformed wide bands [14], with spectral bands such as 2.65–2.9 μm and 4.25–4.5 μm considered spectral detection windows for aerial targets. However, these studies focused more on the results or phenomena of optimization than the causes of the characteristic spectral bands and the effects of instrument performance on the relative difference between the target and background.

In view of the above, this paper builds a simulation model of space-based observed aircraft infrared characteristics and uses B7—12 of Gaofen-5 (GF-5) visual and infrared multispectral sensor (VIMS) [28] data and ground-measured plume data [6] for preliminary validation. A radiative contribution evaluation was carried out to discuss the contributions of background radiation, skin emission radiation, skin reflection radiation, and plume radiation at body-leaving and at-sensor radiance, as well as to analyze the effects of diurnal variation and spatial resolution on the radiative contribution. Then, the effect of instrument performance on the T-B contrast was discussed, and the formation of characteristic spectral bands was analyzed in conjunction with the radiance contribution evaluation and atmospheric attenuation effects. In Section 2, we described the simulation methodology, the flow, and the case of validation and analysis. In Section 3, simulated results were compared with space-based and ground-based data for validation. The contribution of aircraft and background radiation to the body-leaving and at-sensor radiance, and the effect of instrument performance on the T-B contrast, were then assessed. Lastly, the discussions and conclusions are provided in Sections 4 and 5, respectively.

2. Methods and Materials

2.1. Observed Radiance of Aircraft by Space-based Sensor

Within the instrument's linear response range, the measured radiance (also known as restored at-sensor radiance or restored onboard radiance for satellite remote sensing) can be assumed to be the result of a convolution process using an abstract concept of a sensor's equivalent response function and a random noise process, as shown in Formula (1) [29].

$$L_{res\_TOA} = L_{TOA} \otimes R_{sensor} + L_{noise} \tag{1}$$

where L_{res_TOA} and L_{TOA} are the restored at-sensor radiance and the true top of atmosphere (TOA) radiance, respectively; R_{sensor} is the sensor equivalent response, including the spatial imaging degradation and the spectral response, L_{noise} is the effective instrument noise radiance.

Due to the long observation distance, the solid angle of the aircraft is usually smaller than the instantaneous field of view, so the aircraft is a sub-pixel target in the space-based imaging system [14,27]. Then, the aircraft radiation signal observed by the space-based sensor includes aircraft and background radiation. The TOA radiance, including the target and background signals, can be expressed in Formula (2).

$$L_{TOA} = \tau_{atm}^{H\to TOA}\left(\frac{\overline{L}_{Tar}S_{Tar} + \overline{L}_{Bkg}^{H}S_{Bkg}}{\mathrm{d}^2}\right) + L_{pth}^{H\to TOA} \tag{2}$$

where $\tau_{atm}^{H\to TOA}$ and $L_{pth}^{H\to TOA}$ are atmospheric transmittance and path radiance from the aircraft altitude to the TOA, respectively; $\overline{L}_{Tar}$ and $\overline{L}_{Bkg}^{H}$ are aircraft and background equivalent radiance at flight altitude H, respectively; S_{Tar} and S_{Bkg} are the projected area of the aircraft and background in the viewing direction, respectively; d is the ground sampling distance, assuming that $d^2 = S_{Tar} + S_{Bkg}$.

It is generally believed that the infrared radiation of aircraft mainly comes from skin and plume emission radiation [27]. Besides, the aircraft skin reflected radiance is also taken into account in this paper. The plume is a block of high-temperature gas mass, and the true observed radiation is the coupling of the gas emission radiance and the background or nozzle radiance, as shown in Formula (3).

$$\begin{aligned}\overline{L}_{Tar} &= \frac{\int_{S_{Skin}}(L_{E\_skin}+L_{R\_skin})ds + \int_{S_{Plume}}\overline{L}_{Plume}ds}{d^2} \\ &= \frac{\int_{S_{Skin}}(L_{E\_skin}+L_{R\_skin})ds + \int_{S_{NP}}(L_{E\_plume}+\tau_{Plume}L_{Nozzle})ds + \int_{S_{Plume}-S_{NP}}(L_{E\_plume}+\tau_{Plume}L_{Bkg}^{H})ds}{d^2}\end{aligned} \tag{3}$$

where S_{Skin}, S_{Plume} and S_{NP} are the projected areas of the skin, the plume and the nozzle in the observation direction respectively, assuming that $S_{Tar} = S_{Skin} + S_{Plume}$; L_{E_skin} and L_{R_skin} are the emitted radiance and reflected radiance of the aircraft skin, respectively; $\overline{L}_{Plume}$, L_{E_plume}, L_{Nozzle} and L_{Bkg}^{H} are plume equivalent radiance, plume gas emission radiance, nozzle emission radiance, and background radiance at the flight altitude, respectively; τ_{Plume} is the abstract transmittance of the plume gas.

The restored onboard radiance of the aircraft under the space-based infrared observation can be obtained by substituting Formulas (2) and (3) into Formula (1), as shown in

Formula (4). The TOA radiance signal can be simplified into five parts: skin emission radiation, skin reflection radiation, plume radiation, background radiation, and atmospheric path radiation, as shown in Figure 1.

$$\begin{aligned} L_{res\_TOA\_TB} &= \left(\begin{array}{c} \frac{\tau_{atm}^{H\to TOA}}{\mathrm{d}^2} \left(\int_{S_{Skin}} (L_{E\_skin} + L_{R\_skin}) ds + \int_{S_{NP}} (L_{E\_plume} + \tau_{Plume} L_{Nozzle}) ds \right. \\ \left. + \int_{S_{Plume}-S_{NP}} (L_{E\_plume} + \tau_{Plume} L_{Bkg}^{H}) ds + \int_{S_{Bkg}} L_{Bkg}^{H} ds \right) + L_{pth}^{H\to TOA} \end{array} \right) \otimes R_{sensor} + L_{noise} \\ &= \underbrace{\left(\frac{1}{d^2} \int_{S_{Skin}} L_{E\_skin}^{TOA} ds + \frac{1}{d^2} \int_{S_{Skin}} L_{R\_skin}^{TOA} ds + \frac{1}{d^2} \int_{S_{Plume}} \overline{L}_{Plume}^{TOA} ds + \frac{1}{d^2} \int_{S_{Bkg}} L_{Bkg}^{TOA} ds + L_{pth}^{H\to TOA} \right)}_{TOA\ Radiance} \otimes R_{sensor} + L_{noise} \end{aligned} \quad (4)$$

where $L_{E\_skin}^{TOA}$, $L_{R\_skin}^{TOA}$, $\overline{L}_{Plume}^{TOA}$ and L_{Bkg}^{TOA} are the radiance of the skin emission, reflected radiance, plume radiance and background radiance reaching the sensor, respectively.

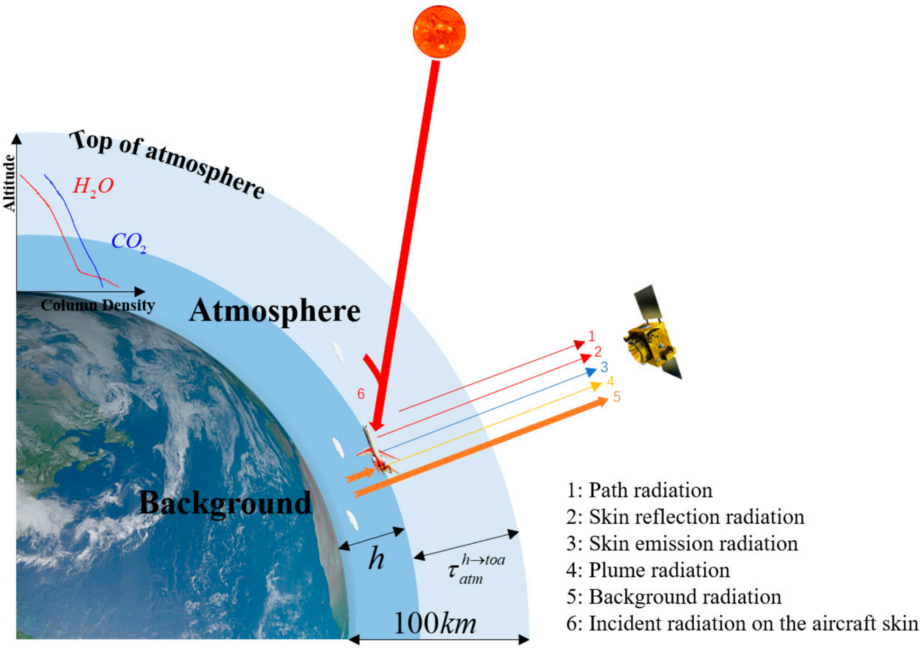

Figure 1. Diagrammatic sketch of aircraft infrared observation using space-based sensors. Schematic CO_2 and H_2O column density diagrams with altitude are in the upper left corner.

2.2. The Flow and Metrics of Analysis

Space-based observed aircraft infrared radiation is affected by aircraft radiation, background radiation, atmospheric effects, and instrument performance. To further investigate the causes of space-based observed aircraft infrared radiation, a quantitative assessment of the various impact factors should be carried out. As shown in Figure 2, the research framework in this paper is as follows: Firstly, a model of aircraft space-based infrared observation radiation was developed, coupling aircraft radiation, background radiation, atmospheric effects, and instrument performance characteristics. Preliminary validations were carried out using space-based data and plume static measurement data. Then, based on the simulation model, the contributions of the skin emitted/reflected radiation, plume radiation, background radiation, and path radiation were calculated and evaluated at the aircraft body-leaving radiance and at-sensor radiance. Finally, the effects of GSD, MTF, *SRF*, and noise on T-B contrast were analyzed regarding the current level of instrument performance.

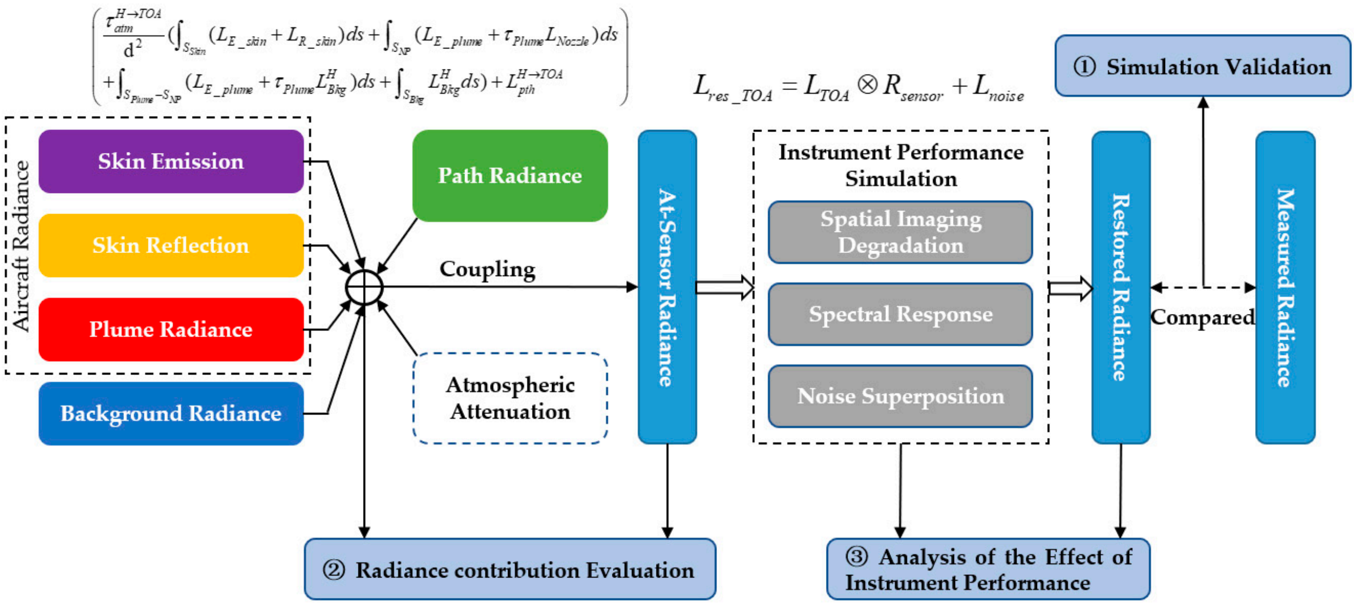

Figure 2. The flow chart of evaluation and analysis in this study.

The simulation results were compared with the restored onboard radiance [29]. Then the absolute error (AE) and relative error (RE) were adopted to evaluate the simulation accuracy, as shown in Formulas (5) and (6) [29]. T-B contrast was adopted to assess the relative difference and relationship between the aircraft observed radiance and the background radiance. The contrast can be calculated by Formula (7) [30], and a positive number means that the aircraft is brighter than the background. The light-dark relationship in the simulation data was also used as a model reliability assessment metric. Another metric to assess the model's reliability is the consistency of the T-B light-dark relationship between measurements and predictions. The absolute mean values of these metrics were likewise calculated, as shown in Formula (8).

$$AE_i = L_{ONBOARD,i} - L_{SIMU,i} \tag{5}$$

$$RE_i = \left(1 - \frac{L_{SIMU,i}}{L_{ONBOARD,i}}\right) \times 100\% \tag{6}$$

$$CR_i = \left(\frac{L_{TB,i}}{L_{Bkg,i}} - 1\right) \times 100\% \tag{7}$$

$$|MEAN| = \begin{cases} \frac{1}{n}\sum_i^n \left|1 - \frac{L_{SIMU,i}}{L_{ONBOARD,i}}\right| \times 100\% & MRE \\ \frac{1}{n}\sum_i^n \left|L_{ONBOARD,i} - L_{SIMU,i}\right| & MAE \\ \frac{1}{n}\sum_i^n \left|\frac{L_{TB,i}}{L_{Bkg,i}} - 1\right| & MCR \end{cases} \tag{8}$$

where AE_i, RE_i, CR_i, $L_{SIMU,i}$ and $L_{ONBOARD,i}$ are the absolute error, relative error, T-B contrast, simulated radiance and restored onboard radiance of the i-band, respectively; $L_{Bkg,i}$ is the background radiance; $L_{TB,i}$ is the radiance of the pixel containing the target and background; MRE, MAE and MCR are the mean relative error, the mean absolute error and the mean contrast ratio, respectively; n is the number of bands.

To validate the accuracy of pure aircraft (without background) simulation and its influence on the reliability of the overall simulation model, an attempt was made to separate the influence of background radiance. Assuming that the measured signal of the aircraft is linearly mixed from the pure target signal and the background signal at the pupil, it can be expressed as Formula (9).

$$\xi_{TB} = (1 - F) \cdot \xi_{Bkg}^{Toa} + F \cdot \xi_{Tar}^{Toa} \quad (9)$$

where ξ_{TB} is the aircraft observed signal, including both aircraft and background signals; ξ_{Bkg}^{Toa} and ξ_{Tar}^{Toa} are the pure background and aircraft signals at the TOA, respectively; F is the aircraft signal factor, describing the contribution ratio of the target signal to the observed signal. The measured background radiance and the aircraft projected area ratio S_{Tar}/d^2 can be used to estimate ξ_{Bkg}^{Toa} and F for the calculation of ξ_{Tar}^{Toa}, which can be compared with the simulation results of the aircraft without the background.

The spectral relative contribution (RC) of the aircraft skin emission radiance, reflected radiance, plume radiance, background radiance, and path radiance to the total body-leaving radiance and at-sensor radiance for the aircraft are calculated separately by Formula (10). In particular, the path radiance accounts for the flight altitude to the top of the atmosphere, which mainly affects the at-sensor radiance. The analysis of each component's relative contribution provides further insight into the role of each radiation source in the different spectral bands and the effect of atmospheric attenuation.

$$RC(\lambda) = \frac{L_{component}(\lambda)}{L_{Tot}(\lambda)} \quad (10)$$

where $L_{component}$ presents radiance components, including the skin emission/reflection radiance, plume radiance, background radiance and path radiance (only for at-sensor radiance) observed at the body-leaving radiance and at-sensor radiance; L_{Tot} is the total radiance, including the total body-leaving radiance and at-sensor radiance of aircraft. These coefficients can be derived by Formulas (3) and (4).

The spectral T-B contrast under different instrument performances was calculated to evaluate each performance parameter's effect. Spectral bands with significant and prominent contrast in the target background were selected for further analysis. Finally, in conjunction with the analysis of instrument performance and radiance contributions, the causes of contrast in the characteristic spectral bands were discussed, and the advantages and disadvantages of each of these bands were compared.

2.3. Simulation Modeling

2.3.1. Skin Radiance

Aircraft skin radiance included skin emission and reflected radiance. The airframe is usually made of metal and coated, of which emitted radiance can be calculated using Planck's formula, as shown in Formula (11).

$$L_{E\_skin}(\lambda, T) = \frac{\varepsilon(\lambda) \cdot M_{BB}(\lambda, T)}{\pi} = \varepsilon(\lambda) \frac{2hc^2}{\lambda^5} \frac{1}{e^{ch/\lambda kT} - 1} \quad (11)$$

where ε is the emissivity of the skin; M_{BB} is the blackbody irradiance; T is the temperature; h is the Planck constant; c is the speed of light; λ is the wavelength, and k is the Boltzmann constant.

During navigation, the aircraft skin temperature is mainly influenced by atmospheric aerodynamic heating, and the heating effect of solar radiation is smaller and can be neglected [17]. The stagnation temperature is used to estimate the skin temperature, and the calculation formula can be expressed as in Formula (12) [30].

$$T_s = T_0 \left[1 + r \frac{\gamma - 1}{2} Ma^2 \right] \quad (12)$$

where T_s is the skin temperature; T_0 is the temperature of the atmosphere around the aircraft; r is the recovery coefficient; γ is the specific heat ratio; Ma is the Mach number of flight.

In space-based observation, the skin-reflected radiance mainly considers the direct solar radiance and its scattered radiance, the cloud radiance, and the atmospheric thermal radiance. Defining the latter three as sky radiance, the skin body-leaving radiance can be expressed as:

$$\begin{aligned} L_{skin}^{\uparrow} &= L_{E\_skin} + \rho\left(L_{sd} + L_{sky}^{\downarrow}\right) \\ &= L_{E\_skin} + \rho\left(\frac{E_{sd}}{\pi} + \frac{E_{sky}^{\downarrow}}{\pi}\right) \end{aligned} \tag{13}$$

where ρ is the skin reflectivity, and $\rho + \varepsilon = 1$; L_{sd} and $L_{sky}^{\downarrow}$ are direct solar radiance and sky downward radiance on the aircraft skin, respectively. Direct solar radiance and sky radiance can be estimated using direct solar irradiance E_{sd} and atmosphere downward diffused irradiance $E_{sky}^{\downarrow}$ at a specified horizontal height, which can be derived from "flx" files of MODTRAN [31]. Due to the long distance of space-based observation, the aircraft shape can be simplified to calculate the projected area of the aircraft skin [15].

2.3.2. Plume Radiance

Aircraft nozzle radiance was considered grey body radiation with an emissivity of about 0.9 [10], which can be calculated using Planck's formula. The plume, a non-uniformly distributed high-temperature gas, differs from the gray-body radiation characteristics of the surface. Its emission and absorption effects should be considered, and the radiative transfer equation can be expressed as Formula (14) [32].

$$\frac{dL(s, \vec{s})}{ds} = \kappa_a \cdot \left(L_{BB}(\vec{s}) - L(\vec{s})\right) \tag{14}$$

where κ_a is the absorption coefficient; L is the local radiance, L_{BB} is the blackbody radiance, s and $\vec{s}$ denote the position and optical path vector, respectively.

The LOS method [33] was applied in this study to solve the radiative transfer equation. The non-uniform gas in a line of sight (LOS) is uniformly divided into multiple layers, as shown in Figure 3. Plume gas radiation of a LOS can be expressed as Formula (15). The nozzle or background radiance coupled with the plume gas can be calculated as Formulas (16) and (17), respectively. Thereby, the plume radiation intensity in Equation (3) can be shown as Formula (18).

$$\begin{aligned} L_{E\_plume} &= L_{BB}^{1}(1-\tau_1)\tau_2\tau_3\ldots\tau_n + \ldots + L_{BB}^{i}(1-\tau_i)\tau_{(i+1)}\tau_{(i+2)}\ldots\tau_n \\ &+ \ldots + L_{BB}^{n}(1-\tau_n) \end{aligned} \tag{15}$$

$$\begin{aligned} L_{nozzle\_plume} &= L_{Nozzle}\tau_1\tau_2\tau_3\ldots\tau_n + L_{BB}^{1}(1-\tau_1)\tau_2\ldots\tau_n + \ldots \\ &+ L_{BB}^{i}(1-\tau_i)\tau_{(i+1)}\tau_{(i+2)}\ldots\tau_n + \ldots + L_{BB}^{n}(1-\tau_n) \end{aligned} \tag{16}$$

$$\begin{aligned} L_{bkg\_plume} &= L_{Bkg}^{h}\tau_1\tau_2\tau_3\ldots\tau_n + L_{BB}^{1}(1-\tau_1)\tau_2\ldots\tau_n + \ldots \\ &+ L_{BB}^{i}(1-\tau_i)\tau_{(i+1)}\tau_{(i+2)}\ldots\tau_n + \ldots + L_{BB}^{n}(1-\tau_n) \end{aligned} \tag{17}$$

$$\int_{S_{Plume}} \overline{L}_{Plume} ds = \sum_{i=1}^{M} L_{nozzle\_plume}^{i} \cdot \Delta d^2 + \sum_{j=1}^{N-M} L_{bkg\_plume}^{j} \cdot \Delta d^2 \tag{18}$$

where L_{BB}^{i} is the blackbody radiance of the ith slab; τ_i denotes the transmissivity of the ith slab; $(1-\tau_i)$ is the emissivity of the ith slab, and n represents the number of stratified layers; N is the total number of LOS intersecting the plume; M is the number of LOS intersecting both the nozzle and plume; Δd is the spatial sampling interval of LOS, and the projected area of the plume in the observation direction can be expressed as $S_{Plume} = N \cdot \Delta d^2$.

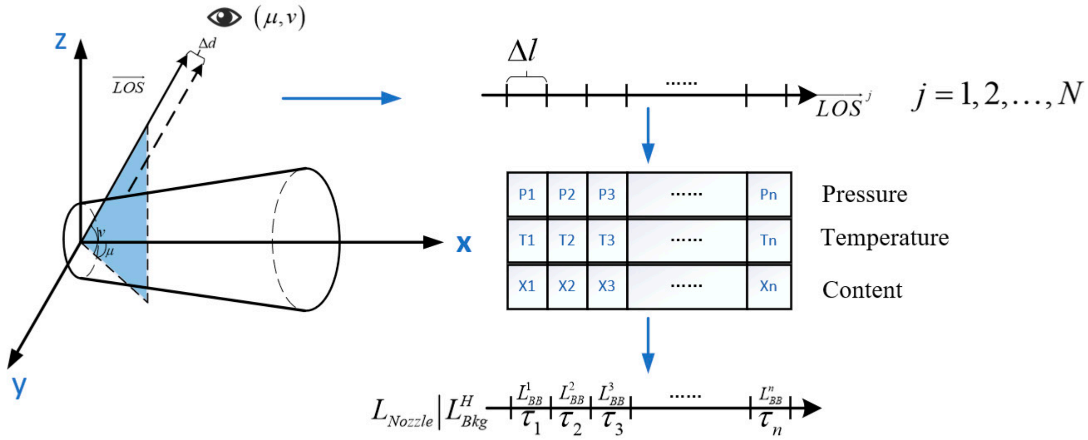

Figure 3. Observation line of sight uniform division schematic. Δl is the length of a slab; N is the total number of sight lines intersecting with the plume; μ and v are the elevation and azimuth angles relative to the aircraft; P, T and X represent the gas pressure, temperature and species content respectively; n represents the number of stratified layers; Δd is the spatial sampling interval of LOS; L_{BB}^n is the blackbody radiance of the n-th slab; τ_n denotes the transmissivity of the n-th slab.

The plume fluid field calculation aims to obtain the gas temperature, pressure distribution, and species content. The computational methods have been divided into two categories. One is the simplified model that uses empirical or semi-empirical formulations to obtain the plume fluid field [34,35]. The other is the computational fluid dynamics that solves the Navier–Stokes equation to derive the plume fluid field [6,32,36]. In contrast to the simplified model, the latter can obtain a fine plume fluid field; however, it requires tedious geometric model construction, meshing, and other manual involvement processes, which costs a large number of computational resources and time. Hence, a simplified model [35] is adopted to complete the calculation of the fluid field distribution.

The absorption coefficients of each species within the specified wavenumber η and temperature intervals can be calculated using the line-by-line method [37] with the aid of the high-temperature database HITEMP [38].

$$\kappa(\eta) = \sum_i S_i(\eta, T) F(\eta - \eta_{0i}) \tag{19}$$

where $S_i(\eta, T)$ is the line intensity of the ith spectral line at a given wavenumber when the temperature is T; $F(\eta - \eta_{0i})$ is the line shape function of the ith spectral line, usually using the Voigt line function, and η_{0i} is the central wave number of the ith spectral line. The spectral line intensity $S_i(\eta, T)$ can be derived by extrapolation from the reference state line intensity $S_i(\eta, T_{ref})$, as shown in Formula (20).

$$S_i(\eta, T) = S_i(\eta, T_{ref}) \frac{Q(T_{ref})}{Q(T)} \exp[\frac{hcE''}{k} \left(\frac{1}{T_{ref}} - \frac{1}{T} \right)] \frac{1 - \exp(-hc\eta/kT)}{1 - \exp(-hc\eta/kT_{ref})} \tag{20}$$

where T_{ref} is the reference temperature; Q represents the partition function; E'' is the lower-state energy of the transition.

2.3.3. Background Radiation Calculation and Instrument Performance Simulation

The background at-sensor radiance can be expressed as Formula (21) [39], considering the atmospheric adjacency effect with the assumption of a flat subsurface. In the infrared band (>2.5 μm), the atmospheric adjacency effect contributes a relatively small amount of radiation to the at-sensor radiance [29]. Thus, the scattered or reflected radiance from ground thermal radiation influenced by adjacency effects is neglected, as shown in Formula (22). The unknown quantities can be calculated by calling MODTRAN several times [40].

$$\begin{aligned} L_{Bkg} &= \frac{A'\rho_t}{(1-\rho_b S)} + \frac{B'\rho_b}{(1-\rho_b S)} + C' \\ &+ \frac{A''\rho_t}{(1-\rho_b S)} + \frac{B''\rho_b}{(1-\rho_b S)} + C'' \\ &+ \varepsilon_b L_{BB}(T_b)\frac{S\rho_t}{(1-\rho_b S)}\tau_d + \varepsilon_b L_{BB}(T_b)\frac{1}{(1-\rho_b S)}\tau_s + \varepsilon_t L_{BB}(T_t)\tau_d \end{aligned} \quad (21)$$

$$\begin{aligned} L_{Bkg} &\approx \frac{(A'+A'')\rho_t}{(1-\rho_b S)} + \frac{(B'+B'')\rho_b}{(1-\rho_b S)} + (C'+C'') + \varepsilon_t L_{BB}(T_t)\tau_d \\ &= \frac{A\rho_t}{(1-\rho_b S)} + \frac{B\rho_b}{(1-\rho_b S)} + C + \varepsilon_t L_{BB}(T_t)\tau_d \end{aligned} \quad (22)$$

where A' and A'' are coefficients describing solar radiance and atmospheric thermal radiance entering the sensor after reflection from the image-pixel surface, respectively; B' and B'' are coefficients describing solar radiation and atmospheric thermal radiation reflected by the area-averaged ground surface into the sensor, respectively; C' and C'' are coefficients describing solar radiation and atmospheric thermal radiation reaching the sensor after scattering in the atmosphere alone, respectively; S represents the atmospheric spherical albedo; ε_t and ε_b denotes the emissivity of the image-pixel surface and the area-averaged ground surface, respectively; τ_d and τ_s are the direct transmission along the line of sight and the effective transmission along the scattering path, respectively; T_t and T_b represent the image-pixel surface and area-averaged ground surface temperatures, respectively; $A = A' + A''$, $B = B' + B''$ and $C = C' + C''$. In the case of cloud scenes, the physical parameters of the clouds are considered to be uniformly distributed horizontally within a single pixel, and the cloud radiance is acquired by setting the cloud parameters by "ICLD", "CTHIK", "CALT" and "CEXT" in the MODTRAN.

Instrument performance simulations are achieved through spatial imaging degradation, spectral response and noise superimposition. Spatial degradation includes sampling interval degradation and imaging blur, $\tau_{atm}^{h\to toa}\left(\overline{L}_{Tar}S_{Tar} + \overline{L}_{Bkg}^{h}S_{Bkg}\right)/\mathrm{d}^2$ in (2) describes the process of spatial resampling, which can be done by setting the GSD to simulate instrument sampling interval degradation. Imaging blur is caused by factors such as the external imaging environment and the imaging capability of the instrument. The sub-pixel target energy appears distributed into several surrounding pixels [14,27]. During instrumental imaging, the imaging blur can be seen as low-pass filtering of the full imaging chain on the ground scene, evaluated by the MTF or the PSF. Accordingly, the spatial domain imaging blur can be expressed as (23). A Gaussian function (24) is usually employed to fit the point spread function, and the MTF is the modulo of the PSF after the Fourier transform. PSF can be calculated by Formula (25).

$$L_{PSF}(x,y) = L_{TOA}(x,y) \otimes \mathrm{PSF}(x,y) \quad (23)$$

$$\mathrm{PSF}(x,y) = \exp\left(-\frac{x^2}{2\sigma_x^2}\right)\exp\left(-\frac{y^2}{2\sigma_y^2}\right) \quad (24)$$

$$\sigma_x = \sigma_y = \frac{\sqrt{2}}{\pi}\sqrt{\ln\left(\frac{1}{MTF}\right)} \quad (25)$$

The spectral response function is commonly applied to describe an instrument's spectral response characteristics [41]. The effective spectral radiance obtained by the sensor is considered a weighted average of the continuous radiance spectrum and the spectral response function, as shown in Formula (26). Gaussian functions are often used to fit spectral response functions, where a spectral response curve can be solved for a given central wavelength and full width at half maximum (FWHM) by Formulas (27) and (28).

$$L_{SRF\_i} = \frac{\int_{\lambda_1}^{\lambda_2} L_{TOA}(\lambda) \cdot SRF_{\mathrm{i}}(\lambda)d\lambda}{\int_{\lambda_1}^{\lambda_2} SRF_{\mathrm{i}}(\lambda)d\lambda} \tag{26}$$

$$SRF_i(\lambda) = \frac{1}{\sqrt{2\pi}\sigma_i} e^{\frac{-(\lambda - CWL_i)^2}{\sigma_i^2}} \tag{27}$$

$$\sigma_i = \frac{FWHM_i}{2\sqrt{2\ln 2}} \tag{28}$$

where L_{SRF_i}, SRF_{i}, CWL_i, $FWHM_i$ are the spectral radiance, spectral response function and its central wavelength and full width at half maximum of the i-band, respectively.

Noise superposition is achieved based on noise equivalent radiance [42], which is modeled by adding a normally distributed random number to each band radiance, as shown in Formula (29). The NEΔT is applied to gauge the noise level of the instrument. Each band's noise equivalent radiance (*NER*) can be calculated from the NEΔT given at the instrument's design, as shown in Formula (30).

$$L_n(i) = L_{TOA} + NER(i) \times rnd\ (\mu = 0, \sigma = 1) \tag{29}$$

$$NER(i) = \frac{L_{BB}(T_B + \Delta T, i) - L_{BB}(T_B, i)}{\Delta T} NE\Delta T(i) \tag{30}$$

where $L_n(i)$ denotes the i-band noise radiance; T_B is the blackbody temperature that NEΔT is defined, and ΔT is the Planck function linear temperature difference.

2.4. Materials for Simulation Case Study

The space-based observed aircraft infrared characteristics model obtains the simulated aircraft observation radiance by inputting information such as ground reflectivity, temperature, and aircraft parameters. Two simulation experiments were designed to validate the model's fidelity; one using satellite-based data to validate the space-based observation simulation model for aircraft; and the other using ground-based measurements of the plume to validate the accuracy of the plume modeling, complementing the former. The simulation time and aircraft parameters from the validation of the space-based observation model were also used in the evaluation of the aircraft observed radiance contribution and the impact of instrument performance.

The onboard data gathered by the VIMS of GF-5 satellite were selected as a reference for the simulation validation, mainly to verify the simulation accuracy in the infrared segment. The VIMS provides images in 12 bands from the visible to thermal infrared, six of which were used for validation in this study. The central latitude and longitude of the chosen data are 32.212895°N and 126.392002°E, located in the East China Sea and imaged on 25 June 2019, with the specific parameters shown in Table 1.

The aircraft's position in the data is shown in Figure 4a, and the aircraft is located above the cirrus, followed by the contrail. The Flightradar24 historical data query shows that the aircraft is a Boeing 777-246, flying from Tokyo, Japan, to Shanghai, China, with an altitude of 12,192 m and a flight speed of 218.64 m/s. The specific parameters are shown in Table 2.

Table 1. Imaging information and instrument performance parameters of GF-5 VIMS.

Parameters	Values
Imaging time (UTC)	25 June 2019 4:38:54
View zenith (°)	179.76
View azimuth (°)	164.25
Band number	B7–B12
Band range	B7:3.45–3.90μm B8:4.76–4.96μm B9:8.05–8.45μm B10:8.57–8.93μm B11:10.5–11.3μm B12:11.4–12.5μm
GSD (m)	40
NEΔT (K)	0.15K@300K
MTF	0.15

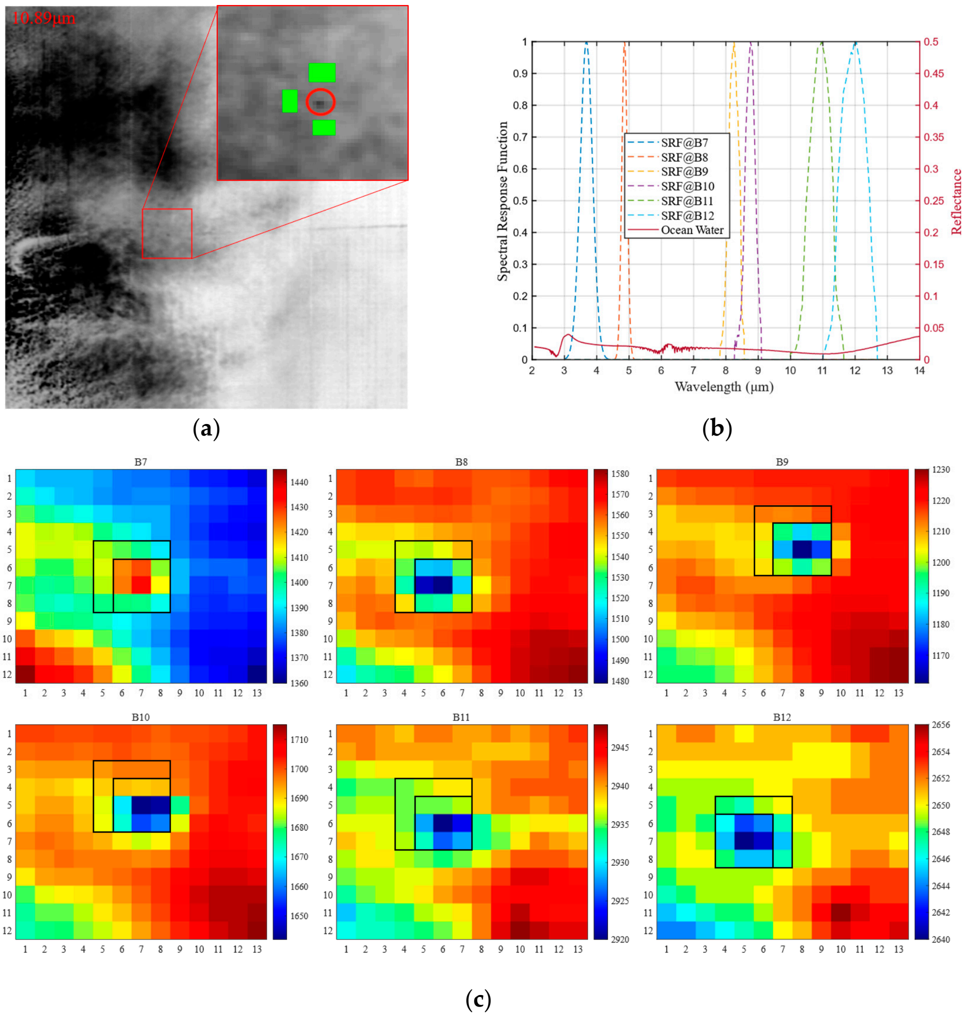

Figure 4. Auxiliary data for simulation, (**a**) aircraft position (red circle), the green box is selected cloud background area; (**b**) spectral response functions of B7–B12 and sea surface reflectance; (**c**) aircraft position and pixel aggregation information for B7–12 images.

Table 2. Aircraft information.

Parameters	Values	Parameters	Values
Aircraft type	Boeing 777-246	Wing area (m^2)	427.8
Flight altitude (m)	12,192	Fuselage radius (m)	3.1
Flight speed (m/s)	218.64	Nozzle radius (m)	0.57
Fuselage Length (m)	63.7	Nozzle number	2

As shown in Figure 4c, it is not guaranteed that the aircraft is in a given pixel, and its position is inconsistent between different bands due to inter-band offsets. Accordingly, the target signal needs to be extracted band by band. To ensure that the aircraft signals are within a single pixel for simulation validation, the 3 × 3 and 4 × 4 pixel sizes were merged (shown in the black box in Figure 4c) to obtain the mixed signals at 120 m and 160 m spatial resolution.

The sea surface temperature was obtained from the SST CCI data of ECMWF [43] as 295 K. The sea surface reflectance was used from the ECOSTRESS spectral library [44], and the skin emissivity was set to 0.6 [45]. The aircraft skin is considered a Lambertian body with emissivity and reflectivity summed into one. The cloud thickness at the aircraft location was inverted using MODTRAN and the measured cloud data (average of the green areas in Figure 4a). Under the cirrus assumption, the cloud base and top altitudes are 8.1 and 9.2 km, at which point the simulation results are closest to the measured results.

The main purpose of the simulation validation experiment was to examine the ability to simulate the space-based observational characteristics of the pixel containing the aircraft, and the spectral response was considered to describe the VIMS instrument performance. The spectral response functions of the B7–B8 were generated based on the spectral ranges given in Table 1 with Gaussian functions, and the B9–B12 spectral response functions were provided by the Numerical Weather Prediction Satellite Application Facility [46], as shown in Figure 4b.

As the VIMS cannot capture the infrared spectral characteristics of the aircraft plume, such as 4.2 µm, the Swedish Defense Research Agency's engine plume measurements [6] were applied to validate the aircraft plume model. The plume simulation considered the effect of CO_2 and H_2O, with the gas velocity of Mach 0.6, the ambient atmospheric temperature of 290 K, the atmospheric pressure of 101 kPa, air humidity of 35% and detection distance of 20 m perpendicular to the plume. Horizontal path atmospheric attenuation and path radiation were also considered.

3. Results

3.1. Validation of the Simulation Results

3.1.1. Space-Based Simulation Validation

The simulation results of the aircraft-observed radiation for space-based infrared observations were validated by the B7–12 data from VIMS, as shown in Figure 5. The background (green box in Figure 4a) spectral mean and its distribution were calculated and compared with the simulation results, as shown in Figure 5a. The 3 × 3 and 4 × 4 pixel size resampling were selected to extract the aircraft observed radiance spectra (containing both aircraft and background), which were compared with the simulation results as in Figure 5b. The comparison results of aircraft and background spectra curves are given in Figure 5c, d. The results show that the measured radiance and T-B relationship agree with the established model.

In order to quantify the errors between simulations and measurements, the relative and absolute errors at different spatial scales and the T-B contrast were calculated, respectively, as shown in Table 3. The MRE of the aircraft observation characteristics simulations for 3 × 3 and 4 × 4 pixel sizes are 8.32% and 6.42%. The maximum contribution of RE is the B7 band (−28.46%, −20.40%), which has low radiance with sensitivity to errors, as corroborated by the AE. Compared with the simulation accuracy of aircraft observation characteristics, the RE of pure aircraft simulation is larger. The MREs of pure target simulation are 71.22% and 56.71%, and the maximum contribution of RE is B7 (161.95%, 123.92%). Besides, the simulated and measured cloud backgrounds were also compared as shown in Figure 5a, with an MRE of 4.52%.

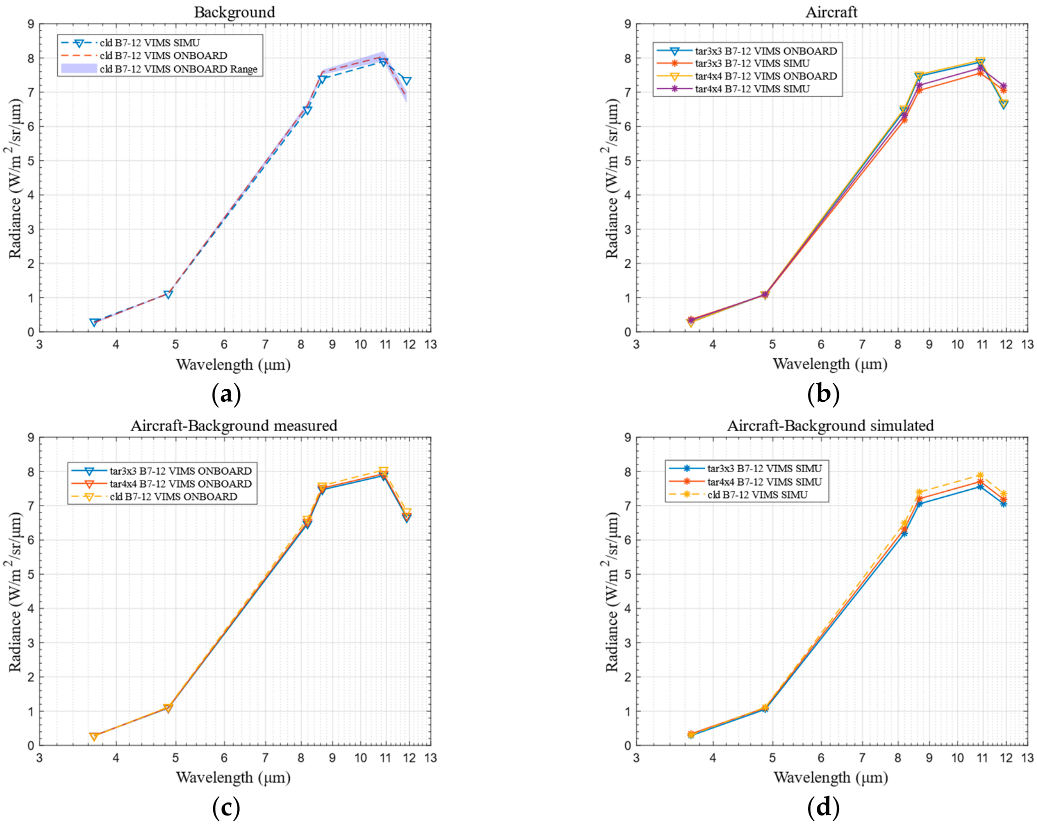

Figure 5. The comparison of the background and aircraft radiance spectra, (**a**,**b**) is the comparison of simulated and measured restored radiance, and (**c**,**d**) is the comparison of target and background radiance curves.

Table 3. Simulation accuracy, target-background contrast calculation results.

Band	Aircraft 3 × 3		Pure Aircraft 3 × 3		T-B Contrast 3 × 3	
	RE	AE	RE	AE	Onboard	Simulation
B7	−28.46%	−0.0810	161.95%	0.8563	5.54%	20.57%
B8	1.47%	0.0161	−20.64%	−0.1269	−2.61%	−3.24%
B9	4.34%	0.2804	−69.48%	−2.7987	−2.26%	−4.67%
B10	5.56%	0.4152	−73.91%	−4.0741	−1.58%	−4.65%
B11	4.08%	0.3218	−60.80%	−3.1544	−2.05%	−4.28%
B12	−6.04%	−0.4017	−40.55%	−1.471	−2.71%	−4.08%
∣MEAN∣	8.32%	0.2527	71.22%	2.0802	2.79%	6.91%
Band	**Aircraft 4 × 4**		**Pure aircraft 4 × 4**		**T-B contrast 4 × 4**	
	RE	**AE**	**RE**	**AE**	**Onboard**	**Simulation**
B7	−20.40%	−0.0573	123.92%	0.7665	4.20%	11.57%
B8	0.74%	0.0081	5.98%	0.0275	−1.91%	−1.82%
B9	3.12%	0.2039	−67.18%	−2.5168	−1.41%	−2.63%
B10	4.13%	0.3106	−72.90%	−3.8681	−0.98%	−2.61%
B11	2.83%	0.2248	−55.15%	−2.5014	1.41%	−2.41%
B12	−7.27%	−0.4871	−15.10%	−0.3834	2.04%	−2.29%
∣MEAN∣	6.42%	0.2153	56.71%	1.6773	1.99%	3.89%

This phenomenon indicates that the accuracy of the overall model is more dependent on the background simulation because the aircraft contribution is smaller. Therefore, the MRE decreases and converges to the background simulation accuracy (MRE of 4.52%), along with the spatial resolution decreases. Meanwhile, it can be found that the simulation accuracy of pure aircraft also changes with the scale (it should not change theoretically), which shows a deviation in the estimation of the aircraft signal factor. There may be two reasons for this deviation. One is that there are unknowns or deviations in aircraft parameters, such as the observation angle of the aircraft, the actual size, etc., resulting in the inability to estimate the aircraft signal factor effectively; the other is that the aircraft projected area ratio may introduce errors.

Objectively, most of the research on infrared signature analysis is controlled by military research institutions with limited details in the open literature [47]. The lack of target-related data, especially measured space-based infrared data for the aircraft, is an important factor restricting the validation and improvement of space-based infrared imaging simulation models. Accordingly, the consistency of the T-B relationship between measurements and predictions can also be used to evaluate the reliability of the simulation model. The simulation and the measured T-B contrast results show that the aircraft observed radiance in the B7 band is higher than the background (brighter than the background), while the opposite is true in other bands. This phenomenon indicates alignment between the simulated and measured T-B relative relationships.

3.1.2. Plume Simulation Validation

Plume infrared characteristic measurement experiments were carried out on the engine test stand [6]. The results were used to validate the plume simulation accuracy and to supplement the space-based observation simulation validation. The comparison between the measured and simulated results is shown in Figure 6. The MRE in the 4.1–5 µm was calculated to be approximately 61.64% (excluding the position of strong atmospheric absorption).

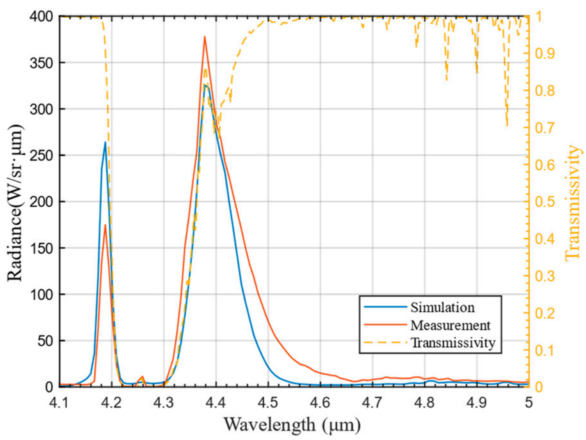

Figure 6. Comparison of plume measurement and simulation and atmospheric transmittance at 20 m horizontal path.

The results show a good agreement between simulation and measurement, with the same spectral characteristics. The partially unknown parameters of the experimental environment have caused errors between the simulation and the experiment. In the reference [4], the spectral radiation intensity is accurate up to 50% after considering all uncertainties associated with the input. By contrast, the simulation accuracy in the paper has been able to achieve a relatively good result with the condition of unknown input parameter uncertainty.

3.2. Evaluation of the Aircraft and Background Contribution to the Observed Radiance

It is widely recognized that background radiation affects the characteristics of aircraft space-based observations, especially at low spatial resolutions where the target features are not obvious mixed with the background radiation. However, it still lacks a quantitative analysis of background and aircraft contributions to observed radiation gathered by space-based infrared sensors. The contributions of each radiance component at 2.5–13 µm were calculated for the body-leaving radiance and TOA radiance at different spatial resolutions and day/night conditions, as shown in Figures 7 and 8. The night scenes mainly considered the absence of solar radiation.

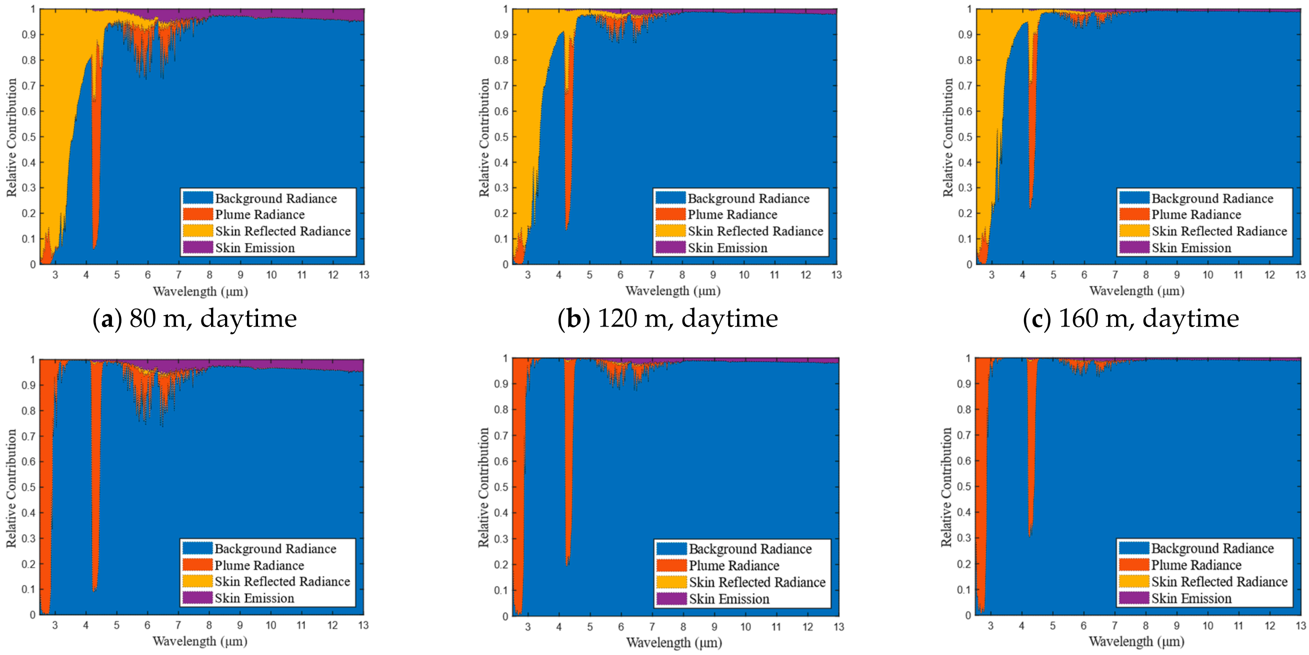

(**a**) 80 m, daytime (**b**) 120 m, daytime (**c**) 160 m, daytime

(**d**) 80 m, nighttime (**e**) 120 m, nighttime (**f**) 160 m, nighttime

Figure 7. Relative contributions for the body-leaving radiance at 2.5–13 µm. (**a**–**c**) are the contribution plots of three spatial resolutions in the daytime; (**d**–**f**) are the contribution plots in the nighttime; the blue, red, yellow, and purple areas represent the relative contribution of the background radiance, plume radiance, skin reflected radiance and skin emission radiance, respectively.

As shown in Figure 7a,c, the contribution of skin-reflected radiance to the body-leaving radiance at 2.5–3 µm is up to 98%, while the plume radiance occupies a smaller proportion but is still higher than the background radiance. Moreover, the plume and skin-reflected radiance also dominate near 4.3 µm, as the atmosphere has a strong absorption effect at these two spectral ranges, resulting in the lower background radiation energy. At all other spectrum bands, the background radiation makes up a large radiative contribution, especially in the long-wave infrared band, where it accounts for more than 90% and up to 99%. As shown in Figure 7d–f, the contribution of background radiation shows the same trend between daytime and nighttime. Still, the contribution of skin-reflected radiance at nighttime could be negligible due to the absence of solar radiation.

As seen in Figure 8, the TOA radiance increases the atmosphere path radiance from the aircraft altitude to the sensor. Atmosphere path radiation is an important component around 4.3, 6, and 9.5 µm, especially at 4.3 µm, where it accounts for up to 100%. Figures 7a–c and 8a–c show that the contribution of plume radiation is reduced compared to that of body-leaving radiance. H_2O and CO_2 are both the main sources of thermal radiation in the plume and the main species of atmospheric attenuation. Therefore, the plume radiation energy is easily attenuated by the atmosphere, which makes it hard to gather signals of the plume from space-based sensors. The skin-reflected radiation is the largest variable in the TOA radiance between daytime and nighttime, which is reduced by the absence of solar radiation, similar to the diurnal variation in the body-leaving radiance.

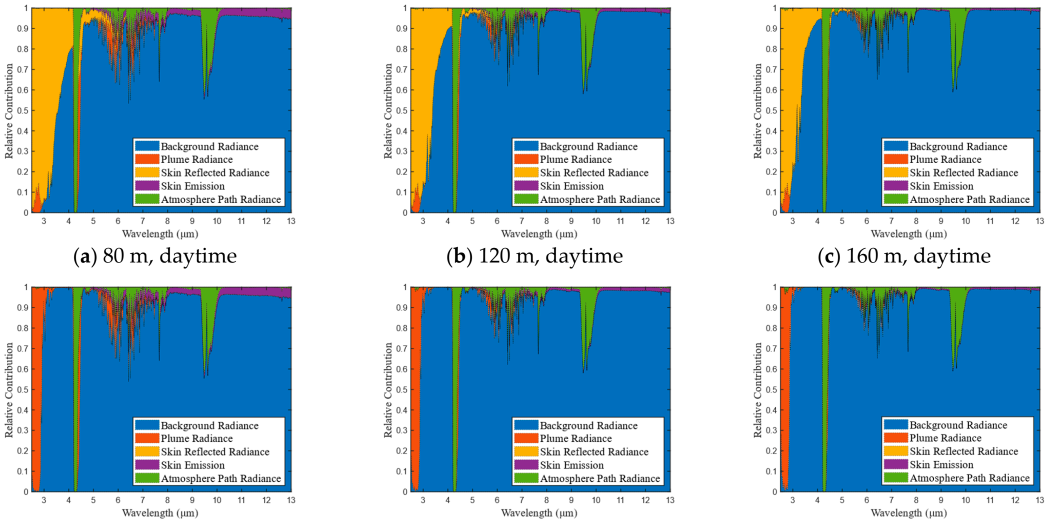

(**a**) 80 m, daytime (**b**) 120 m, daytime (**c**) 160 m, daytime

(**d**) 80 m, nighttime (**e**) 120 m, nighttime (**f**) 160 m, nighttime

Figure 8. Relative contributions for the TOA radiance at 2.5–13 μm. (**a**–**c**) are the contribution plots of three spatial resolutions in the daytime; (**d**–**f**) are the contributions plots in the nighttime; the blue, red, yellow, purple, and green areas represent the relative contribution of the background radiance, plume radiance, skin reflected radiance, skin emission radiance, and atmosphere path radiance respectively.

Jointly, the blue areas of Figures 7 and 8 illustrate that the background radiation has an extremely high radiative contribution overall and increases with GSD. The skin emission radiance is mainly concentrated at 5–13 μm, and its relative contribution decreases with decreasing spatial resolution, from 5% to 1%. The yellow areas in Figures 7 and 8 together illustrate the importance of skin-reflected radiance, which accounts for a high proportion of both the body-leaving and TOA radiance in the daytime. As shown in Figure 9, it is inconsistent with the real relative relationship (Table 3) that the aircraft observed radiance without the skin reflected radiation in the B7 band is lower than the background radiance. This phenomenon highlights the importance and necessity of considering skin-reflected radiance in the simulation model. The diurnal variation of the skin-reflected radiance is also noteworthy. Figure 10 indicates a significant contrast difference between daytime and nighttime, particularly around 2.5–4.15 μm, where the contrast is most significantly reduced and even negative at nighttime. Meanwhile, there is a consistently high level of contrast at 2.7 μm compared with other spectral bands, despite the reduced contrast in the nighttime.

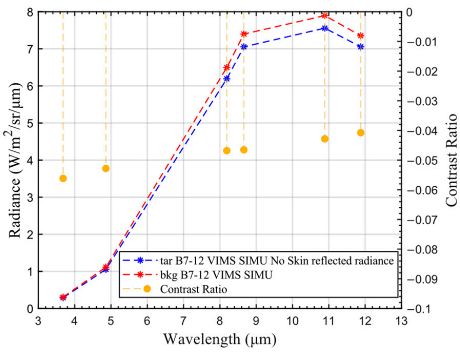

Figure 9. B7–12 radiance comparison of aircraft and background simulated without the skin reflected radiance. The left axis is the radiance, and the right axis is the contrast, where the negative number means that the target radiance is lower than the background radiance.

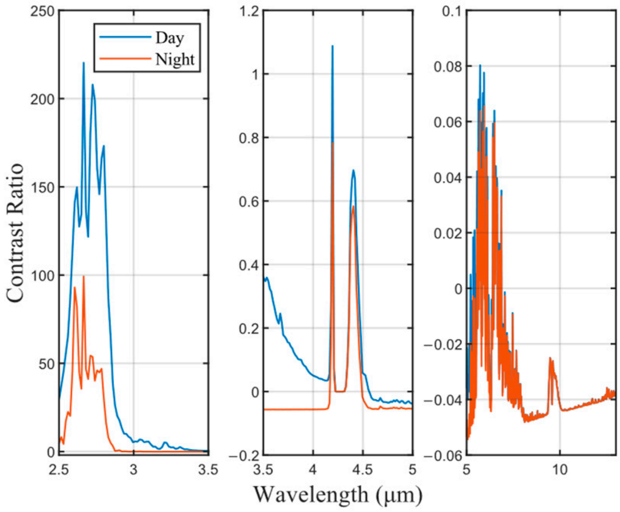

Figure 10. Comparison of target-background contrast ratio in daytime and nighttime.

3.3. Analysis of the Effect of Instrument Performance on Target-Background Contrast

The instrument performance is an important factor affecting the aircraft observation characteristics. For space-based observations with long observation distances, unidentified objects, and unpredictable instrument performance in orbit, it is required to examine the effect of instrument performance parameters on the relative differences between the target and background. The impacts of instrument performance parameters such as GSD, MTF, *SRF*, and NEΔT on the T-B contrast were analyzed according to imaging time, atmosphere, and aircraft parameters in the space-based simulation validation session.

With regard to aircraft space-based observation characteristics, spatial degradation is the most intuitive impact factor. Figure 11 shows the T-B contrast spectra at different GSDs of 70–400 m. The spectral contrasts were shown in three segments due to the large difference between the different spectral ranges. The contrast becomes smaller in absolute terms as GSD increases, with a 97% reduction from 70 to 400 m. Because the lower the spatial resolution is, the higher the background radiance contribution is in the aircraft pixel, which makes the aircraft observed radiance closer to the background radiance. The contrast curves for different MTFs at the GSD of 120 m were presented in Figure 12, demonstrating that T-B relative differences increase with increasing MTF.

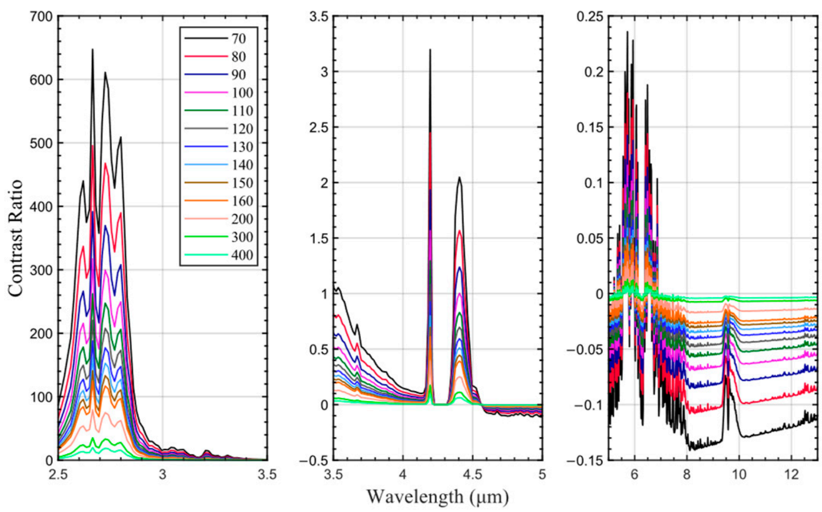

Figure 11. Spectral contrast of target and background at different GSDs of 70–400 m.

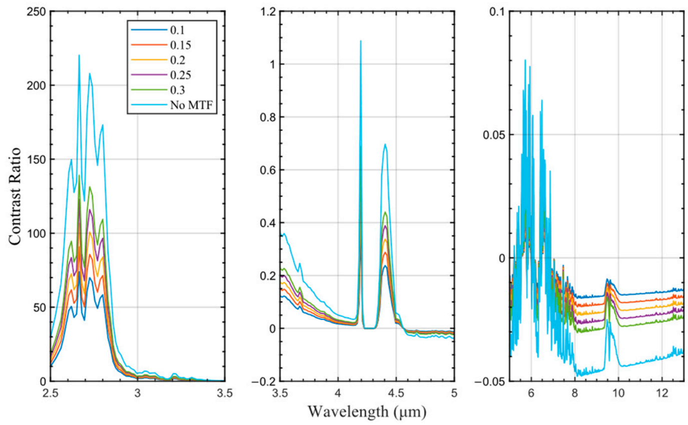

Figure 12. Spectral contrast of target and background at different MTFs of 0.1–0.3.

The results in Figures 11 and 12 show consistently high contrast around 2.7 μm and generally higher contrast at 2.5–3.5 μm than that at 3.5–13 μm. Therefore, 2.7 μm was used in this paper as a general reference for 2.5–3.5 μm. Within 3.5–13 μm, contrast peaks occur around 4.2 μm, 4.4 μm and 5.7 μm. According to Figure 8a–c, it can be found that the skin-reflected radiation and the plume radiation at 2.7, 4.2, and 4.4 μm play a dominant role in making the contrast higher. In comparison, the contrast of 5.7 μm is smaller due to the small contribution of aircraft radiation. Besides, it should be noted that 72% of contrasts are negative at 2.5–13 μm, indicating that the aircraft pixel is darker than the pure background.

Apart from spatial degradation, the instrument's spectral response is a non-negligible influence. The T-B contrast and the *SRF* for VIMS B7–12 at the GSD of 120 m are given in Figure 13. The B7 of VIMS has a central wavelength of 3.68 μm and an FWHM of 0.35 μm. The *SRF* of B7 does not cover the high contrast region of 2.7 μm, so the T-B contrast observed is not high. Meanwhile, the contrast in the spectral response region of the B8-12 is negative, so the aircraft pixel in these bands is darker than the background.

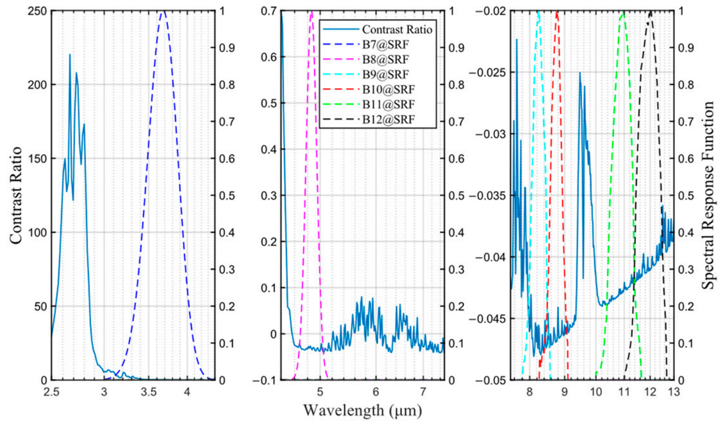

Figure 13. Target-background contrast and the spectral response functions of VIMS B7–12 at the GSD of 120 m.

The above discussion illustrates the importance of designing/selecting the appropriate spectral response region for satellite instruments aiming at aerial target detection. The effect of *SRF* was further analyzed by calculating the T-B contrast for each spectral band at central wavelengths of 2.7, 4.2, 4.4, and 5.7 μm and FWHMs of 0.02, 0.04, 0.08, and 0.16 μm. To account for the impact of spectral calibration error, a random variable with a Gaussian distribution and a standard deviation (STD) of 1 nm was added to the center wavelength. T-B contrast at different central wavelengths and its variation ranges were calculated by several iterations, as shown in Figure 14.

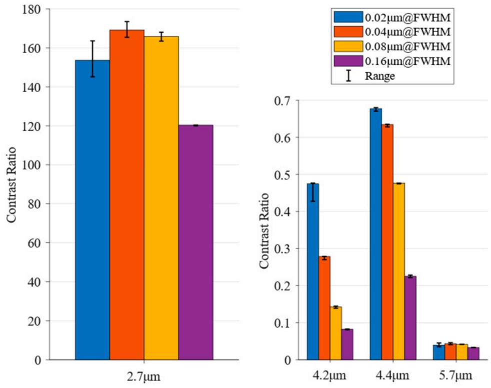

Figure 14. Contrast and its variation range with different center wavelengths and FWHMs.

The contrast is constantly the highest at the central wavelength of 2.7 μm, as shown in Figure 14. The contrast varies inconsistently with the FWHM, indicating that the optimal FWHM for each spectral band is relatively independent. Furthermore, contrast variations caused by central wavelength shifts should be of attention. According to the error bar length, the 2.7 μm contrast variation range is greater and more sensitive to spectral calibration errors. The error bars of the 2.7 μm are equidistant in length between the positive and negative axes, suggesting that the central wavelength could be further optimized to improve the contrast, with the 5.7 μm position showing a similar phenomenon. It is also found that the length of the error bars decreases with the increase of FWHM, indicating that the wider the spectral response range is, the less the contrast is affected by the central wavelength shift. However, an excessively wide spectral response range also reduces the contrast. It is thus essential that the appropriate spectral response is selected while properly controlling the spectral calibration error.

Infrared radiation is less energetic, and remote sensing data is more susceptible to instrument noise compared with the visible. It is often expected that the radiance difference between the target and background exceeds the *NER*, ensuring that the noise does not obscure the target signal. Therefore, this paper compared the T-B radiance difference with the *NER* of VIMS and ASTER instruments [29,48] and analyzed the effect of noise on contrast. Figure 15 shows the T-B radiance difference at the GSD of 120 m and the corresponding *NER* at the NEΔT of 0.15K@300K and 0.3K@300K. The results show that the T-B radiance difference at 4.25 μm, 4.57 μm, and 5–7 μm is less than *NER* with more susceptibility to noise.

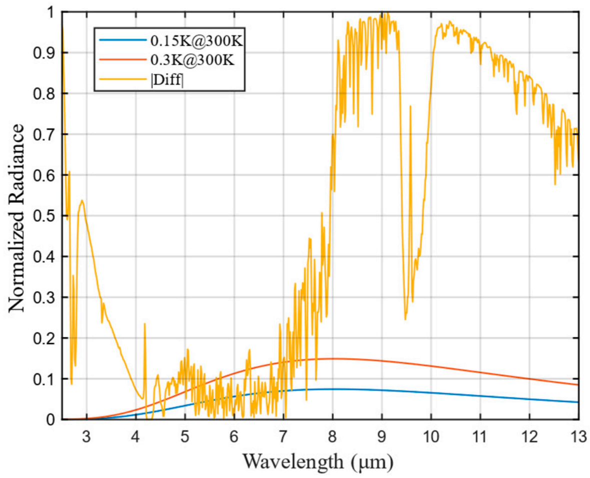

Figure 15. Comparison of noise equivalent radiance and radiance difference between target and background.

The noise was added in the aircraft observed radiation, assuming that the background radiance is the result of averaging over a uniform scene and is not affected by noise. Figure 16 shows the range of variation in contrast and its standard deviation (STD). The results indicate that the standard deviation is greatest, around 2.7 µm, but its effect is almost negligible due to the large contrast. The range of contrast variation around 4.25 µm and 6µm covers the zero axis, indicating a change in the T-B relative relationship (light-dark relationships). It is obvious that a change in the T-B light-dark relationship is not expected, which seriously affects the distinction between the target and background.

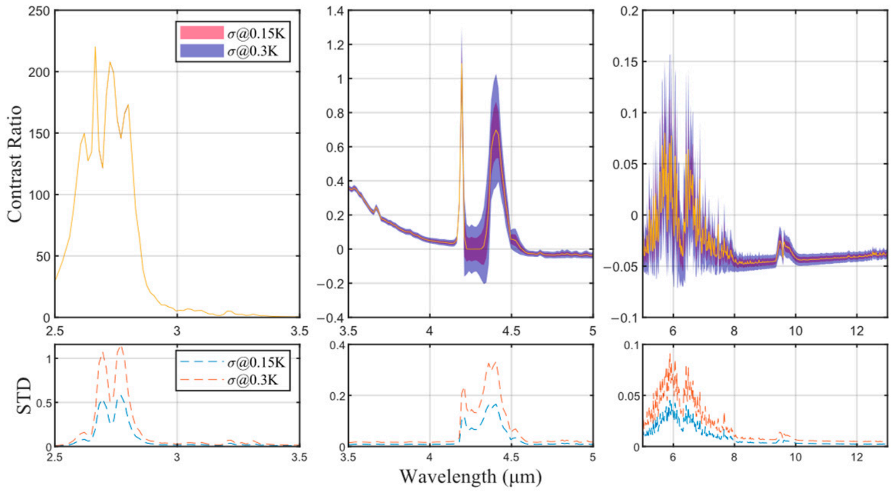

Figure 16. The variation range of target background contrast and its standard deviation curve, considering the influence of noise.

4. Discussions

The validation and evaluation results illustrate that the proposed model can generate accurate simulation data consistent with the measured data. However, the spectral window and challenges for aircraft detection are still open for further discussion.

4.1. Space-Based Infrared Detection Spectral Window for Aircraft

In this paper, aircraft and background radiation contributions are analyzed quantitatively, with a focus on the 2.7 µm, 4.2 µm, 4.4 µm, and 5.7 µm bands as influenced by instrument performance. As seen from Section 3.2, aircraft skin reflections and plume radiance play an important radiance contribution in these spectral bands. This phenomenon indicates that the target-background contrast is higher in the spectral ranges where aircraft radiation makes an important contribution. Because of this, the contrast is consistently higher at 2.5–3.5 µm, where aircraft radiation can contribute up to 98%.

The stronger atmospheric attenuation for the background, in addition to the difference in radiation between the aircraft and the background itself, is an important cause of the higher contrast at 2.7 µm. The atmospheric transmittance from a 0 to 12 km altitude to the TOA and atmospheric profile of CO_2 and H_2O were given in Figure 17. The whole atmosphere transmittance is almost zero around 2.7, 4.3, and 5–8 µm, which limits the Earth's surface radiation (only path radiance remained) observed by satellite remote sensing. It is the lower atmospheric transmittance and the path radiation at 2.7 µm that results in lower background radiation, meaning that only very small aircraft radiation is required to create high contrast. As seen from Figure 17b, the main gas molecules of atmospheric attenuation are distributed at a 0–10 km altitude, which objectively enables some non-atmospheric windows to be detection spectral windows for aerial targets in the air.

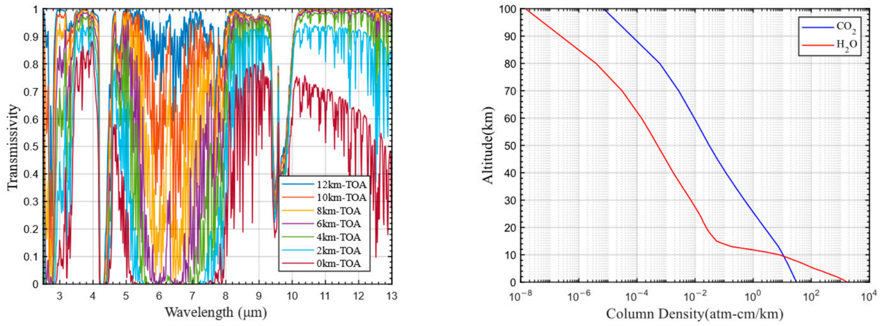

(**a**) (**b**)

Figure 17. Atmospheric transmittance from different altitudes to the top of the atmosphere and atmospheric profile of CO_2, H_2O, derived from output files of the MODTRAN.

The degree of T-B contrast affected by instrument performance varies across the characteristic spectral bands. Undeniably, the T-B contrast around 2.7 μm remains consistently high compared to other spectral bands. From Figures 14 and 16, the contrast at 4.2 μm is more sensitive to FWHM and spectral calibration accuracy, while the contrast at 4.4 μm is more susceptible to instrument noise. Moreover, 5.7 μm does not have a significant advantage compared to other spectral bands.

4.2. The Challenge of Space-Based Infrared Detection of Aircraft

In previous research, aircraft detection could make use of spatial [49], spectral [50], and motion information [2,51] from the aircraft. However, the low energy and long range of infrared remote sensing limit spatial and spectral information applications in detection. Some researchers [23,24,27] used SNR and CSNR to select the feature spectrum bands, which have the potential to detect and track aircraft based on motion characteristics [52,53]. This paper uses radiance contribution analysis to explain why these spectral bands were selected. It then remains doubtful whether aircraft identification can be achieved using a single band. Therefore, the method of aircraft identification for space-based infrared observation is still a challenge. The primary question is what information about the aircraft is used to achieve detection or identification, which affects instrument design and algorithm development.

Both traditional and artificial intelligence algorithms require a certain amount of measured data to achieve feature analysis and training. However, the lack of space-based infrared measurements has limited the study of aircraft detection algorithms. The publicly available infrared datasets are mostly derived from ground-based measurements, and the target size in the images is not representative of space-based observations. It is costly to collect a large-scale dataset with accurate pixel-level annotations [54]. The simulation model presented in this paper has the potential to provide space-based infrared data containing aircraft for feature analysis and network training.

5. Conclusions

In this paper, a simulation model of space-based observed aircraft infrared characteristics is established, coupling target, background radiation, and instrument performance effects. The accuracy of the simulation model was validated by comparing the model predictions with data from space-based and ground-based measurements. Validation results reveal that the measured radiance and T-B relationship agree with the established model. It is also found that the model of space-based observed aircraft infrared characteristics is more dependent on background simulation accuracy. To further understand the causes of the aircraft observed characteristics, the contributions of background radiation, skin reflected/emission radiation, atmosphere path, and plume radiation were evaluated. The evaluation of radiance components indicates that background radiance plays a major role overall, while the observed radiance at 2.5–3 μm is mainly from skin reflection and plume radiance. The lack of skin-reflected radiance decreases the model reliability, and its reduction at nighttime reduces the T-B contrast. The effect of instrument performance parameters on space-based infrared detection was analyzed, and the different changes in contrast on detection windows of 2.7, 4.2, 4.4, and 5.7 μm were highlighted. The results show a consistently high level of contrast at 2.7 μm compared with other spectral bands, although it is susceptible to diurnal variations. The discussions denote that the target-background contrast is higher in the spectral ranges where aircraft radiation makes an important contribution. The difference in T-B self-radiation and the stronger atmospheric attenuation for background contribute to the higher contrast at 2.7 μm.

The model proposed in this paper can provide data for space-based infrared detection algorithm development and onboard instrument performance evaluation. The analysis and discussion based on this model provide insight into the causes of target observation characteristics and the effect of instrument performance on the T-B relative difference.

Author Contributions: Conceptualization, J.L. and G.J.; Data curation, J.L. and B.B.; Methodology, J.L.; Validation, J.L. and Z.L.; Writing—original draft, J.L., L.Y., and Z.L.; Writing—review & editing, J.L., H.Z., X.G., and G.J. All authors have read and agreed to the published version of the manuscript.

Funding: This research was funded by the National Key Research and Development Program of China, grant number 2016YFB0500502 and 2016YFB0500505.

Data Availability Statement: Not applicable.

Acknowledgments: The authors are grateful to the anonymous reviewers for their critical review, insightful comments, and valuable suggestions.

Conflicts of Interest: The authors declare no conflict of interest.

References

1. Kasturi, E.; Devi, S.P.; Kiran, S.V.; Manivannan, S. Airline Route Profitability Analysis and Optimization Using BIG DATA Analyticson Aviation Data Sets under Heuristic Techniques. *Procedia Comput. Sci.* **2016**, *87*, 86–92. [CrossRef]
2. Liu, Y.; Xu, B.; Zhi, W.; Hu, C.; Dong, Y.; Jin, S.; Lu, Y.; Chen, T.; Xu, W.; Liu, Y.; et al. Space Eye on Flying Aircraft: From Sentinel-2 MSI Parallax to Hybrid Computing. *Remote Sens. Environ.* **2020**, *246*, 111867. [CrossRef]
3. Beier, K. Infrared Radiation Model for Aircraft and Reentry Vehicle. In Proceedings of the Infrared Technology XIV, San Diego, CA, USA, 15–18 August 1988; Spiro, I.J., Ed.; SPIE: Washington, DC, USA, 1988; Volume 0972, pp. 363–374.
4. Iannarilli, F.J., Jr.; Wohlers, M.R. End-to-End Scenario-Generating Model for IRST Performance Analysis. In Proceedings of the Signal and Data Processing of Small Targets, Orlando, FL, USA, 1 April 1991; Drummond, O.E., Ed.; SPIE: Washington, DC, USA, 1991; Volume 1481, pp. 187–197.
5. Bishop, G.J.; Caola, M.J.; Geatches, R.M.; Roberts, N.C. SIRUS Spectral Signature Analysis Code. In Proceedings of the Targets and Backgrounds IX: Characterization and Representation, Orlando, FL, USA, 21–25 April 2003; Watkins, W.R., Clement, D., Reynolds, W.R., Eds.; SPIE: Washington, DC, USA, 2003; Volume 5075, pp. 259–269.
6. Johansson, M.; Dalenbring, M. SIGGE, A Prediction Tool for Aeronautical IR Signatures, and Its Applications. In Proceedings of the 9th AIAA/ASME Joint Thermophysics and Heat Transfer Conference, San Francisco, CA, USA, 5–8 June 2006; p. 3276.
7. Cathala, T.; Douchin, N.; Joly, A.; Perzon, S. The Use of SE-WORKBENCH for Aircraft Infrared Signature, Taken into Account Body, Engine, and Plume Contributions. In Proceedings of the Infrared Imaging Systems: Design, Analysis, Modeling, and Testing XXI, Orlando, FL, USA, 5–9 April 2010; SPIE: Washington, DC, USA, 2010; Volume 7662, p. 76620U.
8. Sonawane, H.R.; Mahulikar, S.P. Tactical Air Warfare: Generic Model for Aircraft Susceptibility to Infrared Guided Missiles. *Aerosp. Sci. Technol.* **2011**, *15*, 249–260. [CrossRef]
9. Gangoli Rao, A. Infrared Signature Modeling and Analysis of Aircraft Plume. *Int. J. Turbo Jet Engines* **2011**, *28*, 187–197. [CrossRef]
10. Mahulikar, S.P.; Rastogi, P.; Bhatt, A. Aircraft Signature Studies Using Infrared Cross Section and Infrared Solid Angle. *J. Aircr.* **2021**, *59*, 126–136. [CrossRef]
11. Coiro, E.; Chatelard, C.; Durand, G.; Langlois, S.; Martinenq, J.-P. Experimental Validation of an Aircraft Infrared Signature Code for Commercial Airliners. In Proceedings of the 43rd AIAA Thermophysics Conference, New Orleans, LA, USA, 25–28 June 2012; p. 3190.
12. Coiro, E. Global Illumination Technique for Aircraft Infrared Signature Calculations. *J. Aircr.* **2013**, *50*, 103–113. [CrossRef]
13. Coiro, E.; Lefebvre, S.; Ceolato, R. Infrared Signature Prediction for Low Observable Air Vehicles. In Proceedings of the AVT-324 Specialists' Meeting on Multi-Disciplinary Design Approaches and Performance Assessment of Future Combat Aircraft, NATO, Online, 28 September 2020.
14. Yuan, H.; Wang, X.; Yuan, Y.; Li, K.; Zhang, C.; Zhao, Z. Space-Based Full Chain Multi-Spectral Imaging Features Accurate Prediction and Analysis for Aircraft Plume under Sea/Cloud Background. *Opt. Express* **2019**, *27*, 26027–26043. [CrossRef]

15. Zhu, H.; Li, Y.; Hu, T.; Rao, P. An All-Attitude Motion Characterization and Parameter Analysis System for Aerial Targets. *Infrared Laser Eng.* **2018**, *47*, 168–173.
16. Mahulikar, S.P.; Rao, G.A.; Kolhe, P.S. Infrared Signatures of Low-Flying Aircraft and Their Rear Fuselage Skin's Emissivity Optimization. *J. Aircr.* **2006**, *43*, 226–232. [CrossRef]
17. Mahulikar, S.; Potnuru, S.; Gangoli Rao, A. Study of Sunshine, Skyshine, and Earthshine for Aircraft Infrared Detection. *J. Opt. Pure Appl. Opt.* **2009**, *11*, 045703. [CrossRef]
18. Mahulikar, S.; Vijay, S.; Potnuru, S.; Reddam, D.N.S. Aircraft Engine's Lock-On Envelope Due to Internal and External Sources of Infrared Signature. *Aerosp. Electron. Syst. IEEE Trans.* **2012**, *48*, 1914–1923. [CrossRef]
19. Baranwal, N.; Mahulikar, S.P. Infrared Signature of Aircraft Engine with Choked Converging Nozzle. *J. Thermophys. Heat Transf.* **2016**, *30*, 854–862. [CrossRef]
20. Baranwal, N.; Mahulikar, S.P. IR Signature Study of Aircraft Engine for Variation in Nozzle Exit Area. *Infrared Phys. Technol.* **2016**, *74*, 21–27. [CrossRef]
21. Zhang, J.; Qi, H.; Jiang, D.; Gao, B.; He, M.; Ren, Y.; Li, K. Integrated Infrared Radiation Characteristics of Aircraft Skin and the Exhaust Plume. *Materials* **2022**, *15*, 7726. [CrossRef] [PubMed]
22. Huang, Y.; Cui, X. Modulation of Infrared Signatures Based on Anisotropic Emission Behavior of Aircraft Skin. *Opt. Eng.* **2015**, *54*, 123112. [CrossRef]
23. Yuan, H.; Wang, X.-R.; Guo, B.-T.; Ren, D.; Zhang, W.-G.; Li, K. Performance Analysis of the Infrared Imaging System for Aircraft Plume Detection from Geostationary Orbit. *Appl. Opt.* **2019**, *58*, 1691–1698. [CrossRef] [PubMed]
24. Zhu, H.; Li, Y.; Hu, T. Key Parameters Design of an Aerial Target Detection System on a Space-Based Platform. *Opt. Eng.* **2018**, *57*, 023107. [CrossRef]
25. Yu, S.; Ni, X.; Li, X.; Hu, T.; Chen, F. Real-Time Dynamic Optimized Band Detection Method for Hypersonic Glide Vehicle. *Infrared Phys. Technol.* **2022**, *121*, 104020. [CrossRef]
26. Zhou, X.; Ni, X.; Zhang, J.; Weng, D.; Hu, Z.; Chen, F. A Novel Detection Performance Modular Evaluation Metric of Space-Based Infrared System. *Opt. Quantum Electron.* **2022**, *54*, 274. [CrossRef]
27. Ni, X.; Yu, S.; Su, X.; Chen, F. Detection Spectrum Optimization of Stealth Aircraft Targets from a Space-Based Infrared Platform. *Opt. Quantum Electron.* **2022**, *54*, 1–12. [CrossRef]
28. Zhao, Y.; Dai, L.; Bai, S.; Liu, J.; Peng, H.; Wang, H. Design and implementation of full-spectrum spectral imager system. *Spacecr. Recovery Remote Sens.* **2018**, *39*, 38–50. (In Chinese)
29. Qiu, X.; Zhao, H.; Jia, G.; Li, J. Atmosphere and Terrain Coupling Simulation Framework for High-Resolution Visible-Thermal Spectral Imaging over Heterogeneous Land Surface. *Remote Sens.* **2022**, *14*, 2043. [CrossRef]
30. Shao, X.; Fan, H.; Lu, G.; Xu, J. An Improved Infrared Dim and Small Target Detection Algorithm Based on the Contrast Mechanism of Human Visual System. *Infrared Phys. Technol.* **2012**, *55*, 403–408. [CrossRef]
31. Acharya, P.K.; Berk, A.; Anderson, G.P.; Anderson, G.P.; Larsen, N.F.; Tsay, S.C.; Stamnes, K.H. MODTRAN4: Multiple Scattering and Bidirectional Reflectance Distribution Function (BRDF) Upgrades to MODTRAN. In Proceedings of the Optical Spectroscopic Techniques and Instrumentation for Atmospheric and Space Research III, Denver, CO, USA, 18–23 July 1999; Larar, A.M., Ed.; SPIE: Washington, DC, USA, 1999; Volume 3756, pp. 354–362.
32. Niu, Q.; Meng, X.; He, Z.; Dong, S. Infrared Optical Observability of an Earth Entry Orbital Test Vehicle Using Ground-Based Remote Sensors. *Remote Sens.* **2019**, *11*, 2404. [CrossRef]
33. Niu, Q.; Yang, S.; He, Z.; Dong, S. Numerical Study of Infrared Radiation Characteristics of a Boost-Gliding Aircraft with Reaction Control Systems. *Infrared Phys. Technol.* **2018**, *92*, 417–428. [CrossRef]
34. Ye, Q.; Sun, X.; Zhang, Y.; Zhang, C.; Shao, L.; Wang, Y. Modeling and Simulation of Infrared Radiation from Rocket Plume at Boosting Stage. In Proceedings of the International Symposium on Photoelectronic Detection and Imaging 2009: Advances in Infrared Imaging and Applications, Beijing, China, 24–26 May 2011; Volume 7383, pp. 355–362. [CrossRef]
35. Zhou, G. Optimization of Radiation Model of Infrared Decoy with Neural Network. *J. Phys. Conf. Ser.* **2019**, *1302*, 042027. [CrossRef]
36. Mahulikar, S.; Marathe, A.; Gangoli Rao, A.; Sane, S. Aircraft Plume Infrared Signature in Nonafterburning Mode. *J. Thermophys. Heat Transf.* **2005**, *19*, 413–415. [CrossRef]
37. Modest, M.F. *Radiative Heat Transfer*; Academic Press: Cambridge, MA, USA, 2013.
38. Rothman, L.S.; Gordon, I.E.; Barber, R.J.; Dothe, H.; Gamache, R.R.; Goldman, A.; Perevalov, V.I.; Tashkun, S.A.; Tennyson, J. HITEMP, the High-Temperature Molecular Spectroscopic Database. In Proceedings of the XVI Symposium on High Resolution Molecular Spectroscopy—HighRus-2009, Prague, Czech Republic, 3 September 2008; Volume 111, pp. 2139–2150. [CrossRef]
39. Cota, S.A.; Kalman, L.S. Predicting Top-of-Atmosphere Radiance for Arbitrary Viewing Geometries from the Visible to Thermal Infrared. In Proceedings of the Remote Sensing System Engineering III, San Diego, CA, USA, 1–5 August 2010; Ardanuy, P.E., Puschell, J.J., Eds.; SPIE: Washington, DC, USA, 2010; Volume 7813, p. 781307.
40. Guorui, J.; Huijie, Z.; Na, L. Simulation of Hyperspectral Scene with Full Adjacency Effect. In Proceedings of the IGARSS 2008-2008 IEEE International Geoscience and Remote Sensing Symposium, Boston, MA, USA, 7–11 July 2008; Volume 3, pp. III-724–III-727.

41. Mouroulis, P.; Green, R.O. Spectral Response Evaluation and Computation for Pushbroom Imaging Spectrometers. In Proceedings of the Current Developments in Lens Design and Optical Engineering VIII, San Diego, CA, USA, 26–30 August 2007; Mouroulis, P.Z., Smith, W.J., Johnson, R.B., Eds.; SPIE: Washington, DC, USA, 2007; Volume 6667, p. 66670G.
42. Zanoni, V.; Davis, B.; Ryan, R.; Gasser, G.; Blonski, S. Remote Sensing Requirements Development: A Simulation-Based Approach. In Proceedings of the The ISPRS Commission I Symposium, Denver, CO, USA, 9–12 July 2002.
43. Merchant, C.J.; Embury, O.; Bulgin, C.E.; Block, T.; Corlett, G.K.; Fiedler, E.; Good, S.A.; Mittaz, J.; Rayner, N.A.; Berry, D.; et al. Satellite-Based Time-Series of Sea-Surface Temperature since 1981 for Climate Applications. *Sci. Data* **2019**, *6*, 223. [CrossRef]
44. Meerdink, S.K.; Hook, S.J.; Roberts, D.A.; Abbott, E.A. The ECOSTRESS Spectral Library Version 1.0. *Remote Sens. Environ.* **2019**, *230*, 111196. [CrossRef]
45. Li, N.; Lv, Z.; Wang, S.; Gong, G.; Ren, L. A Real-Time Infrared Radiation Imaging Simulation Method of Aircraft Skin with Aerodynamic Heating Effect. *Infrared Phys. Technol.* **2015**, *71*, 533–541. [CrossRef]
46. EUMETSAT NWP SAF IR_SRF of GF5 VIMS. Available online: https://nwp-saf.eumetsat.int/downloads/rtcoef_rttov13/ir_srf/rtcoef_gf5_1_vims_srf.html (accessed on 8 August 2022).
47. Mahulikar, S.P.; Sonawane, H.R.; Arvind Rao, G. Infrared Signature Studies of Aerospace Vehicles. *Prog. Aerosp. Sci.* **2007**, *43*, 218–245. [CrossRef]
48. Abrams, M.; Hook, S.; Ramachandran, B. ASTER User Handbook. Available online: https://lpdaac.usgs.gov/documents/1319/ASTER_User_Handbook_v4.pdf (accessed on 31 August 2022).
49. Luo, X.; Wu, Y.; Wang, F. Target Detection Method of UAV Aerial Imagery Based on Improved YOLOv5. *Remote Sens.* **2022**, *14*, 5063. [CrossRef]
50. Yao, Y.; Wang, M.; Fan, G.; Liu, W.; Ma, Y.; Mei, X. Dictionary Learning-Cooperated Matrix Decomposition for Hyperspectral Target Detection. *Remote Sens.* **2022**, *14*, 4369. [CrossRef]
51. Heiselberg, P.; Heiselberg, H. Aircraft Detection above Clouds by Sentinel-2 MSI Parallax. *Remote Sens.* **2021**, *13*, 3016. [CrossRef]
52. Stair, A. MSX Design Parameters Driven by Targets and Backgrounds. *Johns Hopkins Apl. Technol. Dig.* **1996**, *17*, 11–18.
53. Cawley, S.J. The Space Technology Research Vehicle 2 Medium Wave Infra Red Imager. *Acta Astronautica* **2003**, *52*, 717–726. [CrossRef]
54. Li, B.; Xiao, C.; Wang, L.; Wang, Y.; Lin, Z.; Li, M.; An, W.; Guo, Y. Dense Nested Attention Network for Infrared Small Target Detection. *IEEE Trans. Image Process.* **2022**, *14*, 8. [CrossRef]